August 2017

Galactic Outflows and Their Correlations with Galaxy Properties at 0.8 < Z < 1.6

Lindsey Whiting
University of Wisconsin-Milwaukee

GALACTIC OUTFLOWS AND THEIR CORRELATION WITH GALAXY PROPERTIES AT $0.8< z< 1.6$

by

Lindsey M. Whiting

A Dissertation Submitted in

Partial Fulfillment of the

Requirements for the Degree of

Master of Science

in Physics

at

The University of Wisconsin-Milwaukee

August 2017

ABSTRACT

GALACTIC OUTFLOWS AND THEIR CORRELATION WITH GALAXY PROPERTIES AT $0.8< z< 1.6$

by

Lindsey M. Whiting

The University of Wisconsin-Milwaukee, 2017
Under the Supervision of Professor Dawn K. Erb

Outflows have been shown to be ubiquitous in galaxies between z = 1 and z=2, and many models and observations have attempted to correlate the absorption line properties of these outflows with morphological characteristics of their host galaxies. In this study, we examined the spectra of 71 galaxies with redshifts $1< z<2$, paying particular attention to the FeII and MgII absorption lines. We plotted the equivalent width, velocity, and maximum velocity of the absorption features against various physical properties of the galaxies, obtained from catalogues created by Skelton et al., (2014) and van der Wel et al., (2012). We confirmed the presence of outflows in our galaxy sample, and found a significant trend between the equivalent width and star formation rate - outflowing gas has stronger absorption lines in galaxies with higher star formation rates.

TABLE OF CONTENTS

LIST OF FIGURES

ACKNOWLEDGEMENTS

This work is based on observations taken by the CANDELS Multi-Cycle Treasury Program with the NASA/ESA HST, which is operated by the Association of Universities for Research in Astronomy, Inc., under NASA contract NAS5-26555. It is also based on observations taken by the 3D-HST Treasury Program (GO 12177 and 12328) with the NASA/ESA HST, which is operated by the Association of Universities for Research in Astronomy, Inc., under NASA contract NAS5-26555. It was conducted in collaboration with Crystal Martin and Riley Peterson of the University of California-Santa Barbara, and with the assistance, encouragement, and guidance of Dawn Erb of the University of Wisconsin-Milwaukee.

Chapter 1

Introduction

In order to understand the evolution of galaxies, it's necessary to also study their surrounding gas. This gas flows into and out of galaxies - a process referred to as the "baryon cycle" - by accretion of the intergalactic medium and powerful outflows, driven by stellar winds, supernovae, and active galactic nuclei.

It has been well established that outflows are present in almost all starburst galaxies in the local universe (Heckman, 2002), and in Lyman-break galaxies at higher redshifts, but their physical mechanisms and effects on galaxy evolution are not fully understood (Steidel et al., 2010). In general, accurate feedback models are difficult because there are many different processes - such as supernovae, protostellar jets, HII regions, stellar winds, and radiation pressure from young stars - that simulations cannot always resolve. High resolution would require them to be precise on a wide range of scales, from intergalactic distances down to individual stars and supernovae. As finer scales are used, and additional feedback mechanisms are included, more and more computing power is needed. Modeling by Hopkins et al. (2012) has shown that any single feedback mechanism alone fails to reproduce the observed winds, so some combination of processes is in fact necessary.

Their new set of numerical models has shown that different feedback mechanisms

can change the wind morphologies. They demonstrate that, with feedback from radiation pressure and a variety of gas heating sources (supernovae, wind shock, and photons), a massive galaxy at $z \sim 2-4$ has a clumpy morphology and violent outflows of dense, cold gas produced by starbursts. This is similar to Muratov's simulation, performed using FIRE (Feedback in Realistic Environments), which evolves large, star-forming molecular clouds to $z = 0$, and, on small scales, models stellar feedback. They find that high-redshift galaxies undergo intense periods of star formation, followed by strong outflows, implying that feedback is strongly time dependent (Muratov et al., 2015).

AGN (active galactic nuclei) and momentum created by star formation seem to be especially important drivers of outflows (Murray et al., 2005). Models by Choi et al. (2016) show that AGN feedback plays the most dominant role in reproducing basic morphologies of observed, massive, early-type galaxies, and also generate strong outflows in the early stages of galaxy evolution, which suppresses star formation. Simulations of the halos of 30 massive galaxies were created by incorporating various physical modules from previous studies to produce four different models – a reference model including all the modules; a model with no black hole and AGN feedback; one with no metal heating effects; and one with thermal instead of ejective SN feedback and no metal enrichment, metal induced heating or cooling, and no early stellar feedback – which were then compared in order to study the role of various feedback mechanisms on the physical properties of the galaxies. Although AGN feedback was found to be the most important, they found it is still necessary to include stellar feedback in order to properly regulate star formation. These four models may overestimate the SFR since they do not include physical mechanisms, like cosmic rays and relativistic AGN jets, which can suppress star formation.

Without radiation pressure, Hopkins' model produces a wind that is no longer clumpy, with hot gas simply venting away from the galaxy. If instead, sources of hot

gas are removed, very little change is observed in the total outflowing mass. Instead of a single wind velocity, like many models predict, they find that there is a wide range in outflow velocity. They conclude that winds in these types of distant galaxies are probably caused by a two step process: 1) UV and IR radiation pressure moves gas particles which are 2) continually accelerated by photons emanating from the entire disk of the galaxy. This is supported by Murray et al. (2011), who propose that cold gas can survive at large radii because, after it is blown out of the galactic disk by radiation pressure, it experiences ram pressure from hot, outflowing gas produced by supernovae. These models suffer from a variety of possible sources of error: they likely underestimate the amount of cold material in the winds, they don't include a realistic IGM so expansion of gas outside the galaxy is likely quantitatively inaccurate, and, like the simulations by Muratov et al. (2015), they do not include cosmic rays which can significantly contribute to pressure support and possibly to outflows in spiral galaxies.

1.1 Regulation of galaxy growth and IGM enrichment by outflows

Outflows are often invoked to explain various aspects of galactic evolution, including the "baryon deficit". Approximately half the baryons galaxies are thought to have contained have not been detected, indicating that they have likely been ejected by outflows in the past and are now in the CGM (Silk, 2003) . This is supported by the mass-metallicity relation observed in local galaxies. Lower mass galaxies appear to have lower metallicities, which suggests that gases are more easily transported from smaller galaxies, having smaller gravitational wells, into the IGM by galactic winds, enriching the IGM's metal content. There must be a process that efficiently removes matter from galaxies since constraints on the enrichment of the IGM and the

mass-metalicity relation based on observations show that material cannot simply be prevented from entering the galaxy in the first place (Aguirre et al., 2001)

The metallicity of a galaxy can be increased by gas expelled by dying stars, and decreased by the ensuing outflows. However, low metallicity in galaxies is not necessarily a sign of high winds since infalls of low-metallicity gas from the IGM can dilute the overall metal content also. A study of $\sim 53,000$ SDSS galaxies at $z \sim 0.1$ found that, if both high and low mass galaxies form similar fractions of stars, more metals are lost by winds from lower mass galaxies, which have smaller gravitational potential wells (Tremonti et al., 2004). Because of this, outflows are commonly used to explain the lack of gas in irregular dwarf galaxies (Dalcanton, 2007).

Suppressing star formation, like removing any infalls, in the models also does not accurately explain galaxy evolution and metallicity - that causes a much larger amount of baryons to be present in the simulated galactic disks than in observations (Kereš et al., 2009b). If stellar feedback is not included in models of galactic evolution, gas cools and forms stars too quickly, leading to extremely massive stars and SFRs much higher than what is actually observed (Kereš et al., 2009a,b). Without strong stellar feedback, the gravitational collapse of gas clouds means that most of the gas forms stars within a few dynamical times (defined as the time it takes for a star to complete one orbit around its galaxy, in years), while in reality, star formation in galaxies is actually fairly slow, requiring a gas consumption time of about 50 dynamical times (see Figure 1.1). The star formation rate per unit area increases faster than the gas density, implying that galaxies with higher gas densities are more efficient at turning their gas into stars (Kennicutt, 1998).

Models have indicated that feedback processes are essential for explaining the low metallicity of smaller galaxies, the relatively high metallicity of the intergalactic medium, the shape of galaxies, and changes in their star formation rates (Muratov et al., 2015). Observations have found cold, outflowing gas in star-forming galaxies

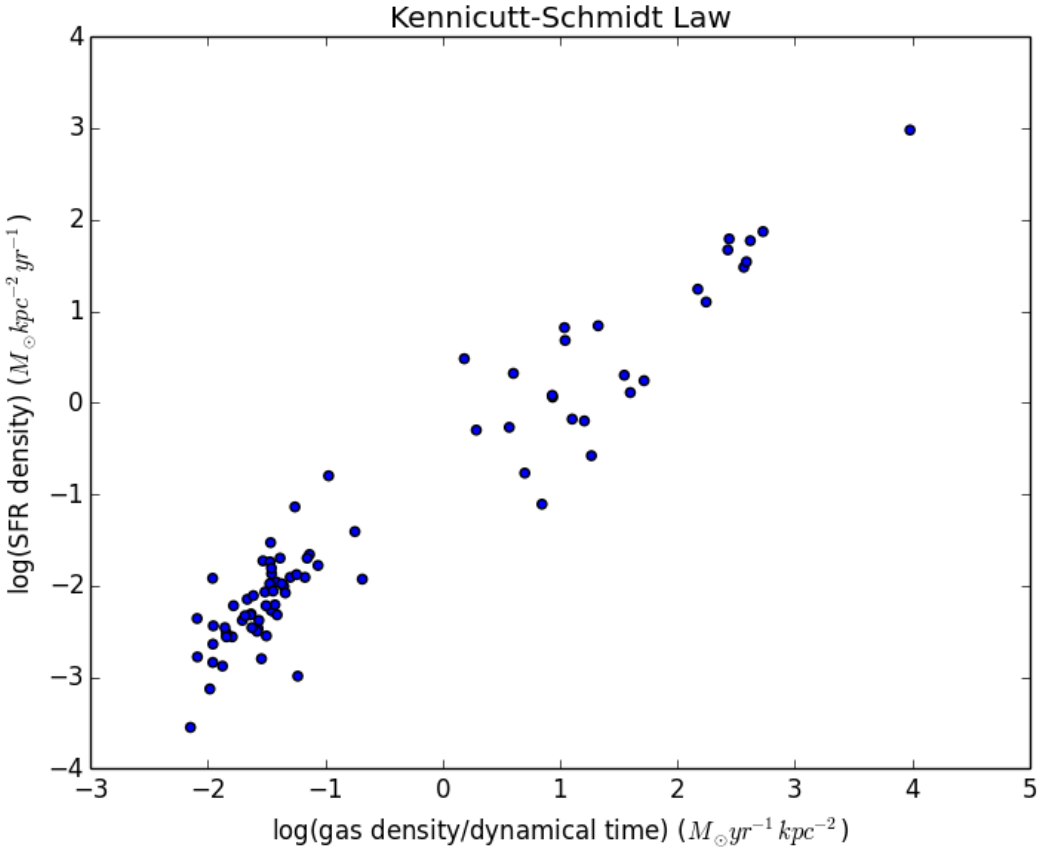

Figure 1.1: A plot of the Kennicutt-Schmidt law created with data from the paper by Kennicutt et al., (1998). That study used a wide range of galaxies, including some with very luminous starbursts. The average dynamical time is about 10^8 years.

.

at a range of redshifts. Radiation pressure from star clusters accelerates cold gas and, when it leaves the galactic plane, it is exposed to hot outflowing gas and radiation. It is then pulled along with the outflows, enriching the IGM (Murray et al., 2011). Since outflows remove gaseous material from the galaxy, they are expected to slow star formation and increase the metallicity of the IGM (Kornei et al., 2012). Studying the metal content of these outflows provides information about the evolution of their host galaxies. Depending on the velocity of the outflow, the expelled material may re-enter the galaxy as inflow, or be completely expelled.

Simulations by Muratov et al. (2015), referenced above, also find that around $z = 2$, galaxies lose about 70% of their ejected material, suggesting that their halos are efficient at expelling gas into the IGM. In particular, strong outflows in dwarf galaxies are able to expel nearly all of the interstellar gas. Infall only replaces a small fraction of the lost material. It appears that, especially for galaxies with massive halos, the CGM acts as a reservoir of enriched gas, which can provide fuel for later stages of galaxy formation.

The most obvious observational indication of the presence of these outflows in distant galaxies is the blueshifting of interstellar absorption lines relative to the redshift of the galaxy. This is caused by outflowing gas along our line of sight to the galaxy absorbing light from the stellar continuum. The velocity shift of the spectral absorption lines can then be used to trace the velocity structure of outflowing gas (Heckman, 2002).

Observations of 89 star-forming galaxies by Steidel et al. (2010) found little evidence for cool inflows into galaxies at $z \sim 2 - 3$. Any infalling gas should be easily detectable by the redshifting of absorption velocities, but, though they found evidence which might be interpreted in support of the presence of infalling gas in massive galaxies, there is no such evidence for low-mass galaxies. However, they did find evidence that suggests high-velocity outflows can deposit material at large radii. This is most

naturally interpreted as gas carried out of the galaxy at an earlier stage of star formation, which would also support Muratov's time-dependent nature of SFR, outflows, and galaxy morphology (Muratov et al., 2015).

1.2 Observations of outflows

Multiple studies of both local (Martin et al., 2012) and high-redshift star-forming galaxies (Weiner et al., 2009) have used blueshifted MgII absorption to observe galactic outflows. MgII provides good information about these outflows because both lines of the $\lambda\lambda$2796 2803 doublet have large oscillator strengths (i.e, high probability of transition between energy levels) and magnesium is fairly abundant in the universe. However, determination of the Doppler shift can be complicated by scattered MgII emission which partially fills in the absorption troughs (Prochaska et al., 2011). Use of bluer FeII absorption lines can provide a better picture since fluorescence instead of resonant emission follows absorption in some of these transitions, so absorption filling doesn't occur (Erb et al., 2012). See Figure 1.2 for an example of some FeII transitions. Observational accuracy can also be limited by spectral resolution of the instrument and a lack of spatial information about the extent of the outflow.

1.3 Correlations of outflow absorption lines with galaxy properties

Previous studies have also tried to determine the drivers of galactic outflows by finding properties of galaxies that appear to correlate with the absorption line velocity shift.

Heckman et al. (2015) analyzed 39 low-z objects with a range of starburst and galaxy properties in order to determine which of these properties correlates with properties of the outflows. The galaxies were chosen from the larger parent samples FUSE

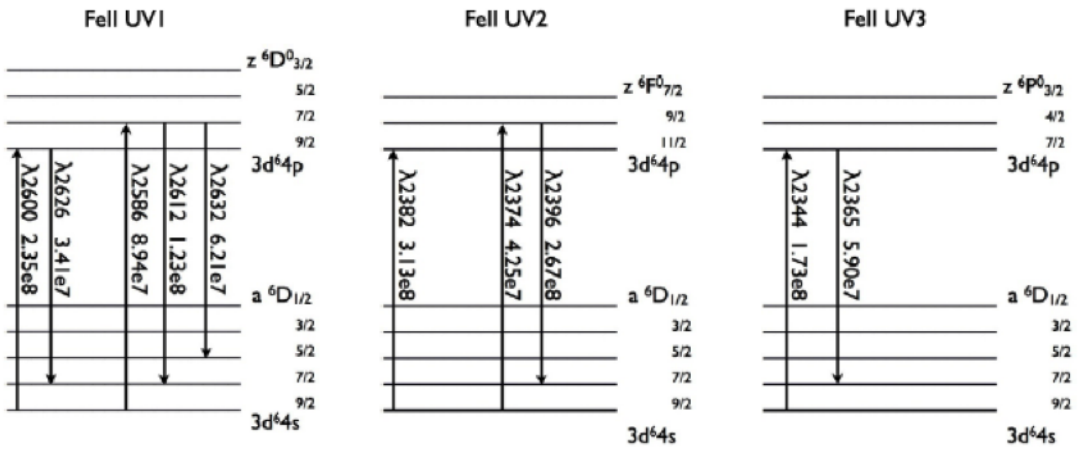

Figure 1.2: An energy level diagram for selected FeII transitions. See Figure 1, "Galactic Outflows in Absorption and Emissions: Near-Ultraviolet Spectroscopy of Galaxies at 1< z< 2", Erb, Dawn K. et al., The Astrophysical Journal 759:26, 2012. ©AAS. Reproduced with permission.
`http://iopscience.iop.org/article/10.1088/0004-637X/759/1/26/meta`

(Far-ultraviolet Spectroscopic Explore) and a cross-match of GALEX (Galaxy Evolution Explorer) and SDSS (Sloan Digital Sky Survey) based on their high S/N and similarity to Lyman break galaxies, which are star-forming galaxies at high redshift chosen based on their appearance in different imaging filters caused by the position of the 912 Å Lyman limit. The galaxies in their sample were then used as analogs to high-z galaxies. They found that outflow velocity, as determined from absorption lines, correlated weakly, if at all, with stellar mass and the circular velocity of the galaxy, but there was a strong correlation with SFR and SFR per unit area. Though they did not investigate any possible time dependence, it is possible to interpret this result in support of the simulations by Muratov et al. (2015) showing that bursts of star formation are quickly followed by gusty outflows at high redshifts.

This is supported by another study of 18 ultraluminous IR galaxies (Martin, 2005) which found that galaxies with higher SFRs accelerate the absorbing clouds to higher velocities. Other observations of low-z objects, however, have been inconsistent. One study was unable to detect any correlations between outflow velocity and physical properties of the galaxies, though there seemed to be a correlation between the equiv-

alent width of the absorption lines and star formation surface density. They posited that the small dynamic range of their sample could be the explanation for the lack of clear trends (Chen et al., 2010).

Local galaxies only have strong winds if intense star formation bursts are also occurring, but at high redshifts, almost all star forming galaxies show evidence of winds (Shapley, 2011). In their $z \sim 1$ observations of 72 star-forming galaxies, Kornei et al. (2012) found a strong correlation between outflow velocity and SFR surface density, and a weak correlation between outflow velocity and SFR, but didn't observe a link between the outflows and galaxy morphology. However, not all galaxies with high star formation rate surface densities exhibited outflows, and the correlation itself appears to be less significant in galaxies with higher redshifts. Since outflows are not always observed in galaxies with high star formation rate surface densities, this appears to be evidence for collimated winds, which would only be visible over a limited range of inclinations. Better resolution galactic images would give a clearer picture of the morphologies and star-forming regions, and more sensitive instruments would allow for better detection of faint outflow emission. The authors believe that these two improvements would make it easier to test these correlations. It is also possible that the observed galaxies have too narrow a range of SFR, so a trend cannot be detected.

Other studies of galaxies at similar redshifts have also found trends: strength of MgII absorption increasing with stellar mass due to more interstellar gas in more massive galaxies which reduces resonant emission (Martin et al., 2012); and tracing gas with higher velocity than the FeII lines, possibly because of emission filling or different oscillator strengths (Kornei et al., 2012). At redshifts around $z = 1.4$, MgII equivalent width, and the outflow velocity, are both larger for galaxies with higher SFR and stellar mass (Weiner et al., 2009).

The results of recent observations have suggested that between $z = 1$ and $z = 2$,

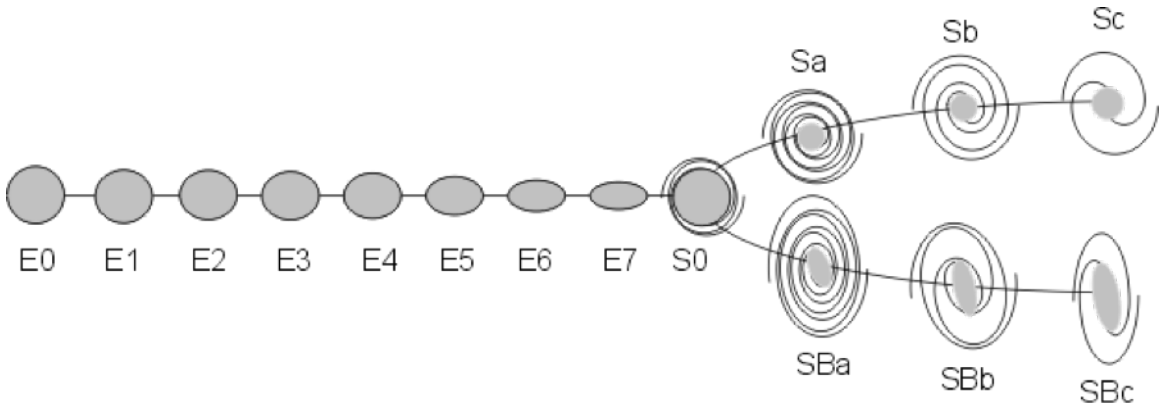

Figure 1.3: The Hubble 'tuning fork' diagram for galaxy classification. Ellipticals (E) are "early-type" galaxies, and spirals (S) are "late-type".

the structure of both the outflows and their host galaxies changes significantly, so this redshift range could provide information about the transformation and evolution of galaxies during this critical period of their existence. Oesch et al. (2010) looked at ~ 8600 galaxies with $0.2 < z < 1$ in the COSMOS field to study the development of the Hubble sequence (see Figure 1.3). They found that the morphological evolution depends strongly on mass - they observed no evolution in galaxies with masses greater than 10^{11} solar masses. For lower mass galaxies, the "early-type" population (elliptical and lenticular galaxies) becomes more important toward lower redshifts, and this is dominated, not by pure ellipticals, but by galaxies with a significant disk component. It seems that the "late-type" galaxies evolve into "early-type" galaxies, and the majority of the time, they become bulge-dominated disks. So at higher redshifts, we would expect to see more "late-type" galaxies, and fewer ellipticals.

Other studies have confirmed this. Around $z = 1$, observations imply that many galaxies have formed disks, and the outflows are well-collimated and perpendicular to them (Kornei et al., 2012; Martin et al., 2012). Some evidence for this - the correlation between outflows and star formation rate surface density - has been discussed above in Section 1.3. The study by Martin et al. (2012) found that at faster speeds, outflows subtend a smaller solid angle. Specifically, they measured outflow speeds of

200, 100, 50, and 0 km s^{-1} at half-angles of 13, 37, 57, and 70 degrees, respectively. By $z = 2$, galaxies are irregular, without a regular spiral structure, and the outflows do not appear to be highly collimated. There is no observable correlation between the inclination of the galaxy - determined by measuring the axis ratios - and the velocity shift of the outflow absorption lines (Law et al., 2012).

1.4 Our goals and the results of similar studies

In this study, we looked at the spectra of 118 galaxies in the redshift range $1 < z < 2$ in order to search for correlations between the strength and velocity of galactic outflows, as measured from the FeII and MgII absorption lines, and the structural properties of the galaxies obtained from HST imaging. Other studies have examined these features in galaxies at similar redshifts and found that the MgII lines range from absorption only, to strong emission, which is more common in galaxies with lower stellar masses (Erb et al., 2012). Martin et al. (2012) found that the strength of MgII absorption in outflows increases with stellar mass, though they did not see any trends in the FeII absorption. Kornei et al. (2013) measured the maximum outflow velocities with FeII and MgII spectral features and found that MgII appeared to trace higher velocity outflowing gas than FeII.

More massive galaxies appear to have less emission filling, which shifts the centroid of absorption lines and reduces their equivalent width (Martin et al., 2012; Prochaska et al., 2011). Kornei et al. (2013) found that FeII* fine structure emission was common in galaxies around $z = 1$ with lower star formation rates. The strongest FeII* emission lines match the systemic velocity of the galaxy, so they may originate in a spatially

extended outflow. These galaxies also tend to have stronger FeII resonant absorption.

Chapter 2

Target Selection, Observations, and Data Reduction

2.1 Target Selection

All the galaxies we obtained spectra for were chosen from the CANDELS survey. CANDELS (Cosmic Assembly Near-IR Deep Extragalactic Legacy Survey) (Grogin et al., 2011; Koekemoer et al., 2011) uses Hubble's Wide Field Camera 3 (WFC3) and Advanced Camera for Surveys (ACS) to image galaxies in five well-studied extragalactic fields. We chose galaxies from two of fields - COSMOS (RA 150.116, DEC +2.201) and EGS (RA 214.825, DEC +52.825), each covering about 0.2 square degrees. Data for each of these fields is available in four different filters - F125W, F160W, F606W, and F814W - with depths ranging from 27.2-28.4. We made an initial galaxy selection, based on data from the 3D-HST catalogue, created by Skelton et al. (2014). They constructed spectral energy distributions (SEDs) for each galaxy in the CANDELS survey and used the EAZY and FAST codes to determine the photometric redshifts and stellar population parameters respectively. We required our objects to have $log(SFR) > 0$, and a photometric redshift between 0.7 and 2, at 99%

confidence. We then prioritized objects with $1< z< 1.6$ so we could calculate systemic redshifts from [OII] emission as well as measure the absorption lines, and an R magnitude ≤ 24 so we could measure absorption lines in each object with sufficient S/N.

2.2 Observations

Our observations were done with the Keck II telescope in Hawaii on March 27-28, 2015 using the DEep Imaging Multi-Object Spectrograph (DEIMOS; (Faber et al., 2003)). DEIMOS is an optical spectrometer with coverage from $\sim 4100 - 11000\mathring{A}$ spanning 16.7x5.0 arcminutes. This range includes rest-frame near-UV features from the FeII absorption feature at 2260 Å to the [OII] emission doublet at 3727 and 3729 Å in galaxies with $1 \leq z \leq 1.7$. We used the 600ZD grating which has a FWHM resolution of 3.5 Å. Using one slitmask for each field, we observed 62 EGS and 56 COS objects. The total exposure time for the COS objects was 9.04 hr and for the EGS objects, 8.79 hr. During our two nights of observation, the sky was very clear, the airmass ranged from 1.31-1.05, and the seeing from 0.81-0.46 arcseconds. At an R magnitude of ~ 24, the average S/N per pixel over the observed (non-rest frame) wavelength range 5000-8000 Å was approximately 2.59 in the COS field, and 3.63 in the EGS field.

2.3 Data Reduction

The collected data was immediately run through the DEEP2 pipeline (Cooper et al., 2012; Newman et al., 2013), which takes care of most of the data reduction. The pipeline first processes the flats and arc lamp images to determine the positions of the slits on the CCD array and solves for the wavelength of each pixel. It then reads in the separate science frames from each chip to extract the data for each slit and

combines the separate exposures into a 2-d, mean, sky-subtracted spectrum. The pipeline also creates a file with all the 2-d spectra, and files with the 1-d spectra for each slit.

Redshifts for each galaxy were measured with [OII] lines, when they were present, which occurred in 30 COS and 41 EGS objects, with mean redshifts of 1.136 ± 0.211 and 1.267 ± 0.226, respectively (see Figure 2.1). The rest of this paper is concerned with only these 71 objects.

Using standard star observations, we put the galaxy spectra on an absolute flux scale and removed the instrumental signature. The spectra were rebinned by a factor of two in order to increase the signal to noise ratio and converted to rest wavelength using the redshift calculated for each individual spectrum. Then, they were normalized in the wavelength range 2000-3000 Å since this area contains the Fe and Mg features we are interested in, and also excludes the noisier red end of the spectra. Using wavelength windows that only contained the continuum, we fit a spline curve to each spectra. We normalized the error spectrum of each object with its corresponding continuum fitting function - examples of this are in Figure 2.2. Figure 2.3 is an example of a composite spectrum made from 96 galaxies in the same redshift range as our sample and it shows the absorption and emission lines we are interested in.

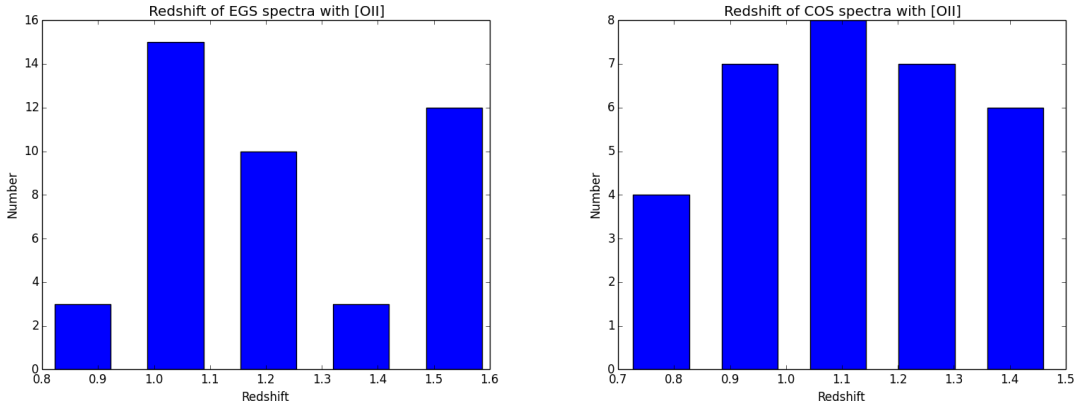

(a) (b)

Figure 2.1: Histogram plots of the redshifts calculated for objects with [OII] present in their spectra at 3727 and 3729 Å.

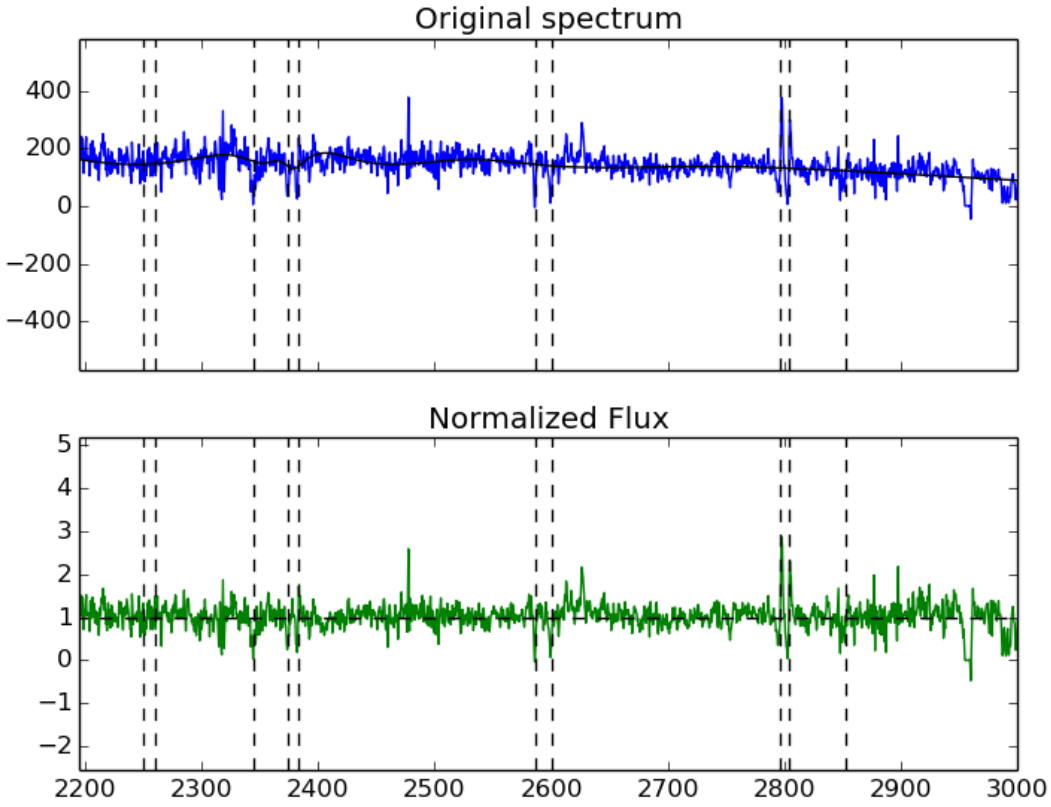

Figure 2.2: Example of spectrum normalization. The top, blue plot is the original flux spectrum with the overplotted black best-fit normalization line. The bottom, green plot shows the results of the normalization. For both plots, the x axis is the wavelength in angstroms, and the y axis is the flux. Vertical dotted lines mark the spectral features we study in our sample.

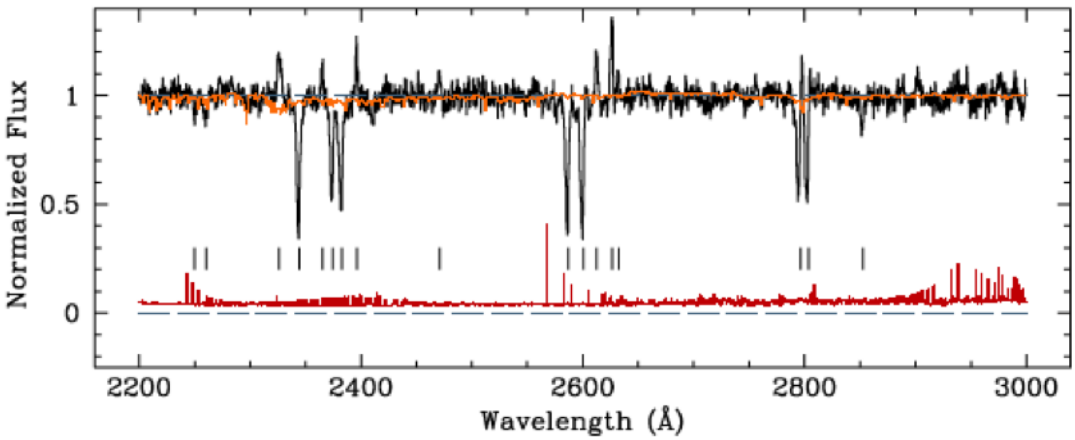

Figure 2.3: An example of a high signal-to-noise, high redshift galaxy spectrum with the features we are interested in measuring marked with vertical lines (see Table 3.1). This is a composite of 96 different galaxies with $1< z< 2$. The red line is the 1σ error spectrum, and the overplotted orange line is the stellar spectrum of a solar metallicity, 100 Myr old galaxy with constant star formation. See Figure 9, "Galactic Outflows in Absorption and Emissions: Near-Ultraviolet Spectroscopy of Galaxies at $1< z< 2$", Erb, Dawn K. et al., The Astrophysical Journal 759:26, 2012. ©AAS. Reproduced with permission.
`http://iopscience.iop.org/article/10.1088/0004-637X/759/1/26/meta`

Chapter 3

Measurements and Conclusions

3.1 Measurements

We measured the equivalent width and velocity relative to the systemic redshift, calculated from the [OII] emission doublet, of the features listed in Table 3.1. First, we found the minimum flux near the expected wavelength of each absorption line (within three pixels), and then searched the spectra in either direction until we reached a flux value that was greater than the continuum. When necessary (for the FeII lines at 2374 and 2382, 2586 and 2600, and the MgII lines at 2796 and 2803), we forced a separation between two features, in case there was no flux value greater than one (the value of the average continuum level in the normalized spectrum) that separated them. Using this information, we calculated the equivalent width of each feature with the equation

$$\mathrm{EW} = D \times \sum_{i=\lambda_{\mathrm{low}}}^{\lambda_{\mathrm{high}}} (1 - f_i), \tag{3.1}$$

where D is the dispersion given by the difference in wavelength between two adjacent data points, λ_{low} is the bluest wavelength of the absorption feature, λ_{high} is is the reddest, and f_i is the normalized flux of the ith pixel.

The equivalent-width-weighted centroid of the line is then given by

$$\lambda_c = \frac{D}{\mathrm{EW}} \sum_{i=\lambda_{\mathrm{low}}}^{\lambda_{\mathrm{high}}} (1 - f_i)\lambda_i, \tag{3.2}$$

and the corresponding velocity centroid is

$$v_c = c\left(\frac{\lambda_c - \lambda_{\mathrm{rest}}}{\lambda_{\mathrm{rest}}}\right) \tag{3.3}$$

where c is the speed of light and λ_{rest} is the vacuum, rest-frame wavelength of the line.

Finally, we calculated the maximum blueshifted velocity of each absorption line, using the lower wavelength limit λ_{low}:

$$v_{\mathrm{max}} = c\left(\frac{\lambda_{\mathrm{low}} - \lambda_{\mathrm{rest}}}{\lambda_{\mathrm{rest}}}\right). \tag{3.4}$$

Then we performed a Monte Carlo simulation by adding a random value, drawn from a Gaussian distribution with width equal to the uncertainty for each pixel, to the data value 1000 different times, and then re-measuring the equivalent width, velocity, and maximum velocity using the perturbed spectrum. The median values of these 1000 measurements are listed in Tables 3.2 and 3.3, along with their error values. The error values for the equivalent width and both velocities were calculated by finding the 68% confidence intervals of the Monte Carlo measurements. We calculated the significance of each equivalent width measurement by dividing the median equivalent width by the error value.

Information on the structural parameters of the galaxies was imported from the catalogue put together by van der Wel et al (van der Wel et al, 2012). These parameters are the results of GALFIT (Peng et al, 2010) Sersic modeling of the galaxies in the CANDELS survey which produces best-fit values for total magnitude, half-light

Ion	λ	Notes
Fe II	2249.88	Absorption
	2260.78	Absorption
	2344.21	Absorption
	2374.46	Absorption
	2382.76	Absorption
	2586.65	Absorption
	2600.17	Absorption
Mg II	2796.35	Absorption and emission
	2803.53	Absorption and emission
Mg I	2852.96	Absorption

Table 3.1: Spectral features we're interested in. The λ column is the vacuum rest wavelength.

radius, Sersic index, axis ratio, and position angle.

We first plotted the FeII absorption lines against each other, and the results are in Figure 3.1. Since these plots show scatter around the 1:1 line, instead of using each individual FeII absorption line on subsequent plots, we plotted the average of the FeII lines for each object. Figures 3.2 - 3.3 show the correlations between the FeII and MgII absorption lines. As seen in previous studies, discussed in the Introduction, the MgII lines have larger blueshifts than the FeII lines, probably because of emission filling.

Plots were made of the physical parameters from the van der Wel and Skelton catalogues (see Tables 3.4 and 3.5) against the equivalent and velocity measurements of our absorption lines, and the results are in Figures 3.4 - 3.9. MgII λ2803 was not included on the maximum velocity plots since its bluest edge is often determined by the artificial, forced separation of the MgII doublet described above.

Spearman correlation coefficients were calculated for each of the above plots and are in Table 3.6. The only significant trend (with a sigma value greater than three) is between equivalent width versus SFR, showing that as the star formation rate increases, there is greater FeII and MgII absorption. This agrees with a study by Weiner et al. (2009), mentioned above, which found that at $z \sim 1.4$, the equivalent

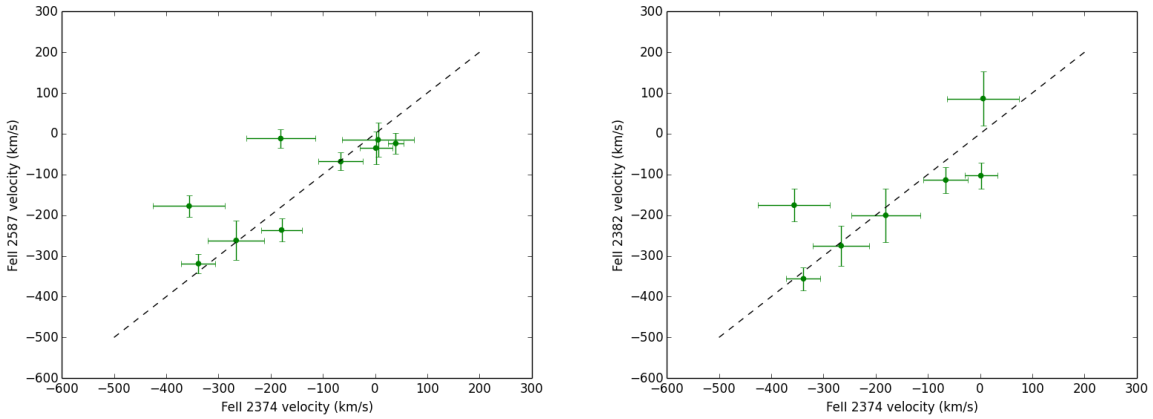

(a)

(b)

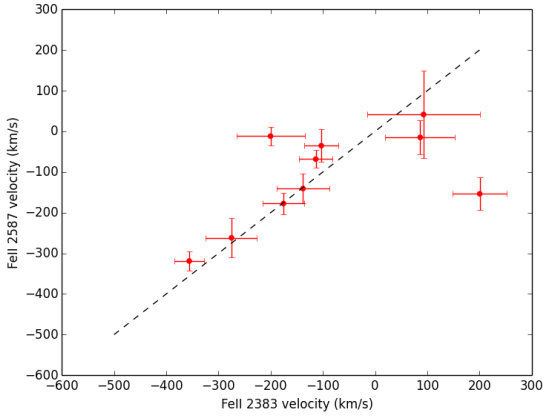

(c)

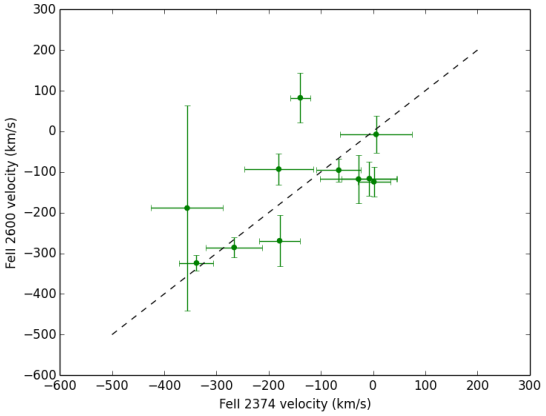

(d)

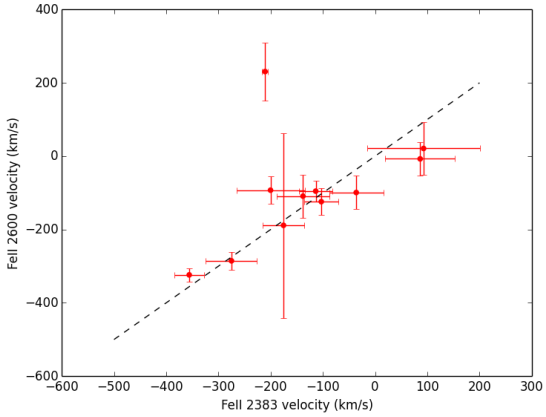

(e)

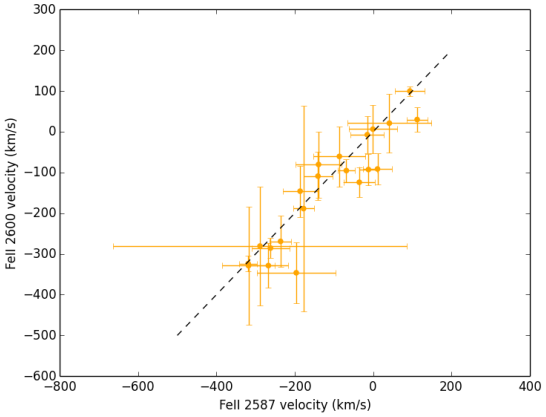

(f)

Figure 3.1: Plots of the FeII lines against each other. The dotted line represents a 1:1 ratio.

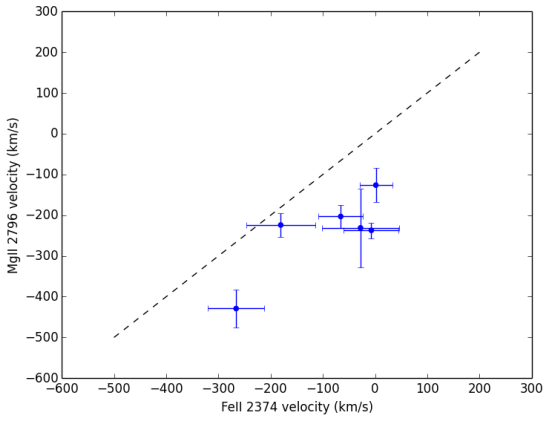

(a)

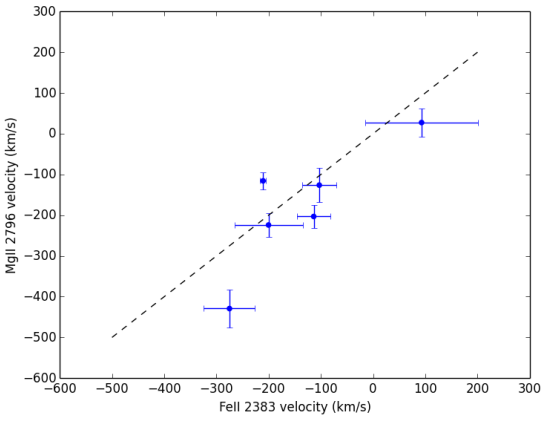

(b)

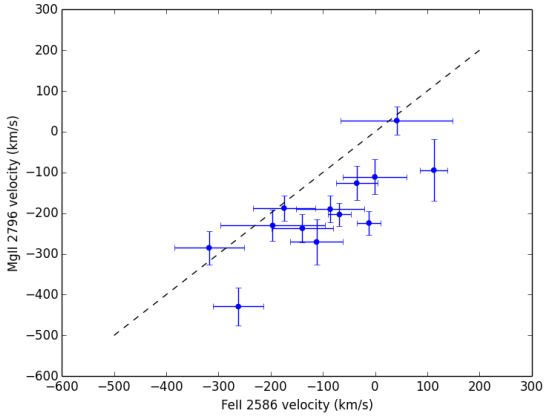

(c)

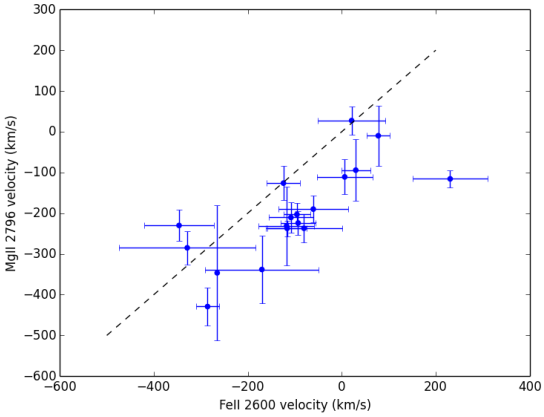

(d)

Figure 3.2: Plots of the FeII and MgII lines against each other. The dotted line represents a 1:1 ratio.

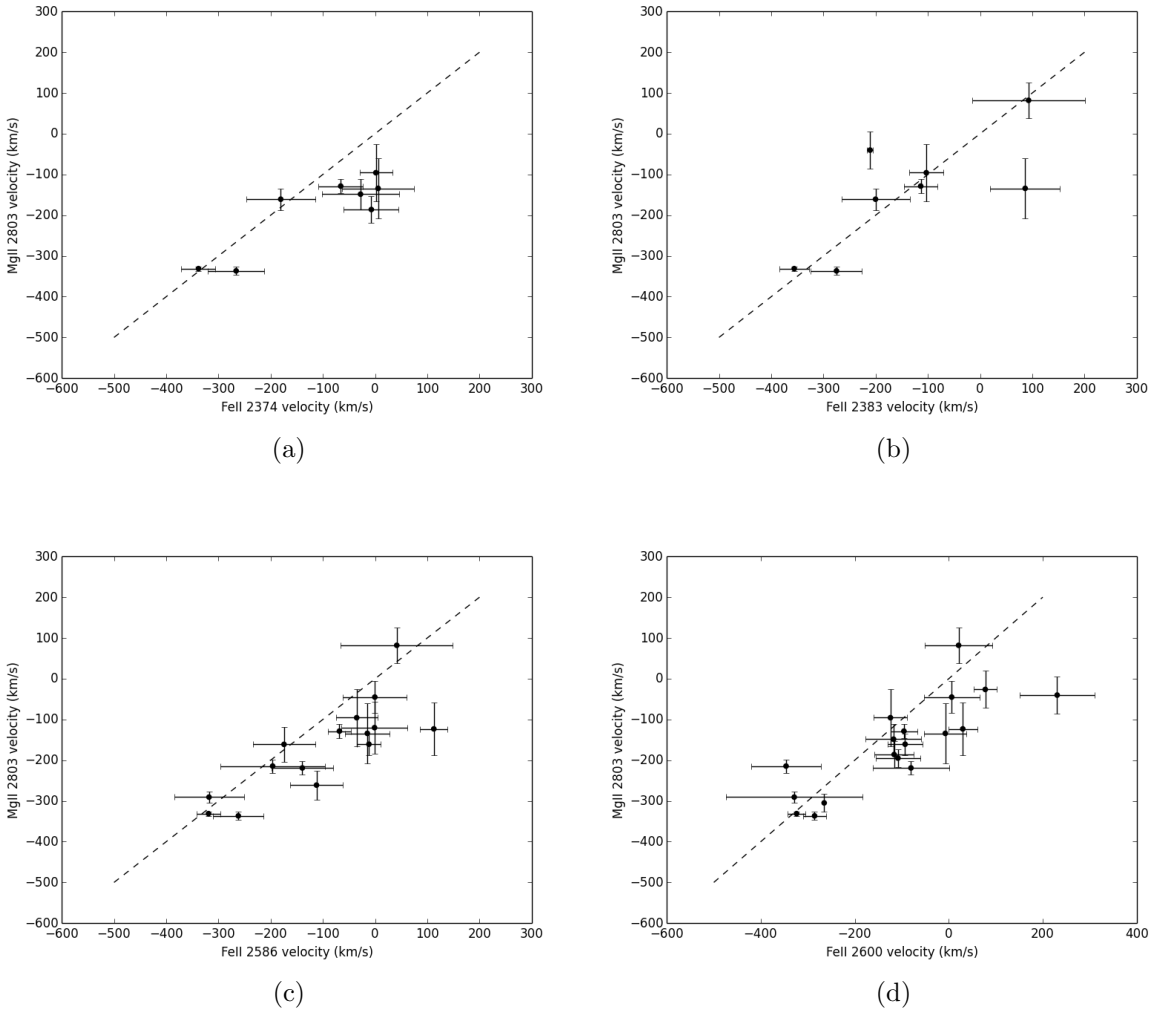

Figure 3.3: Plots of the FeII and MgII lines against each other. The dotted line represents a 1:1 ratio.

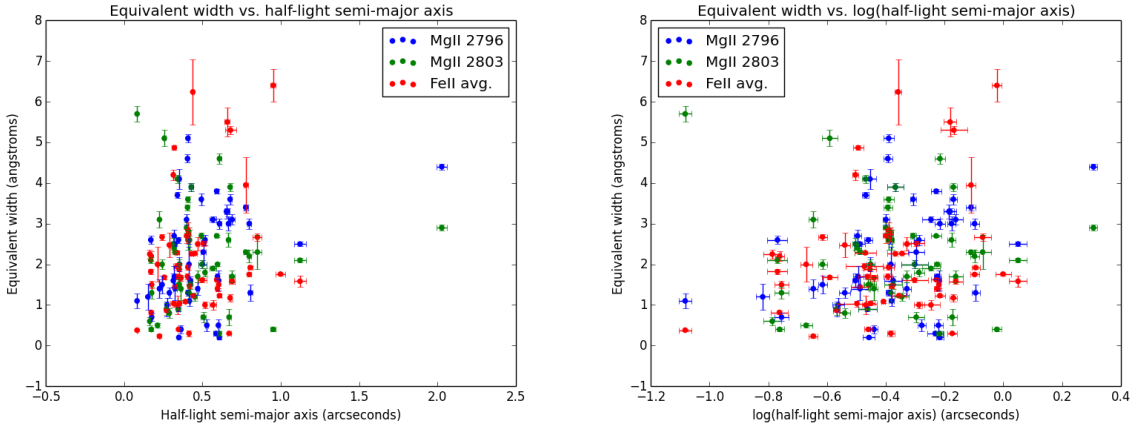

(a) (b)

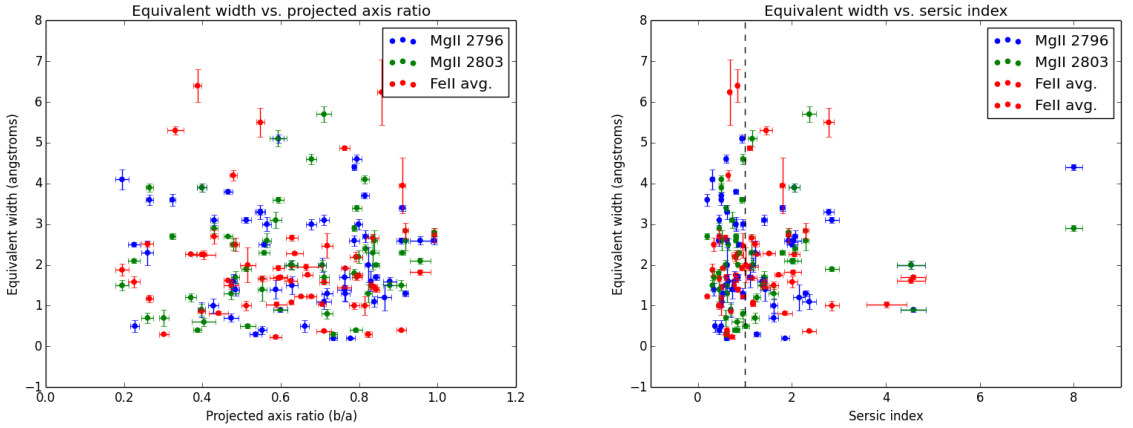

(c) (d)

Figure 3.4: Plots of equivalent width against the van der Wel data.

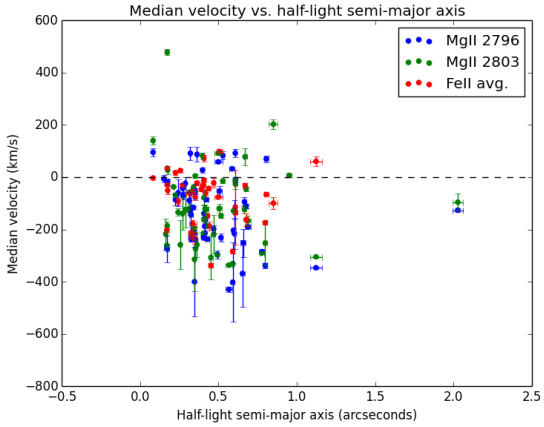

(a)

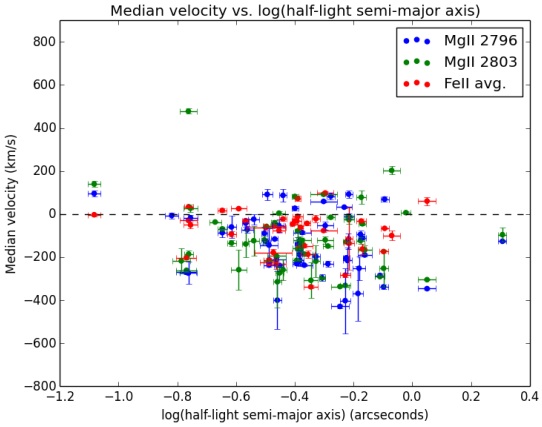

(b)

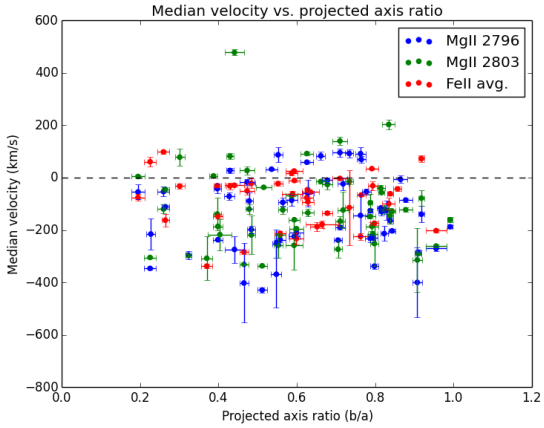

(c)

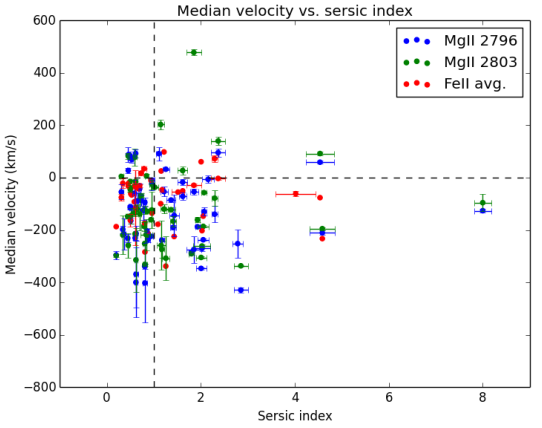

(d)

Figure 3.5: Plots of velocity against the van der Wel data.

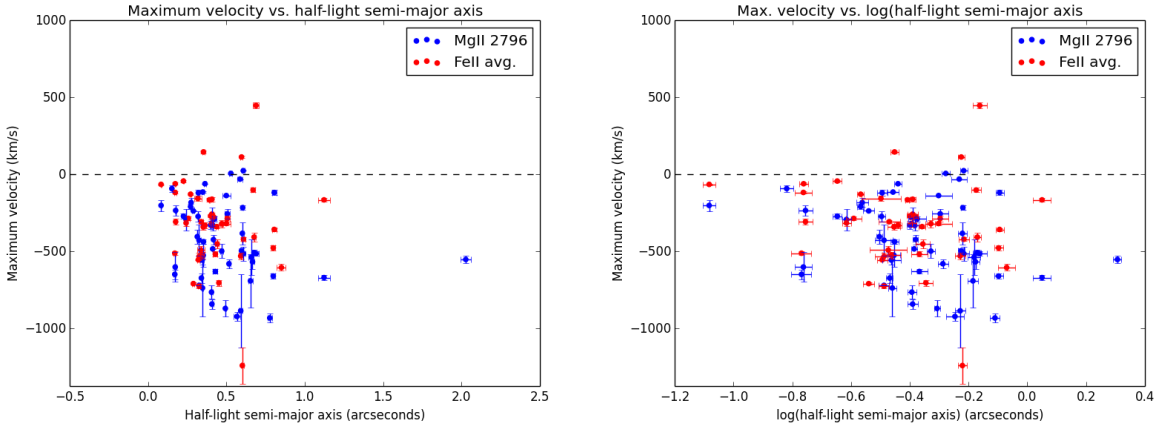

(a) (b)

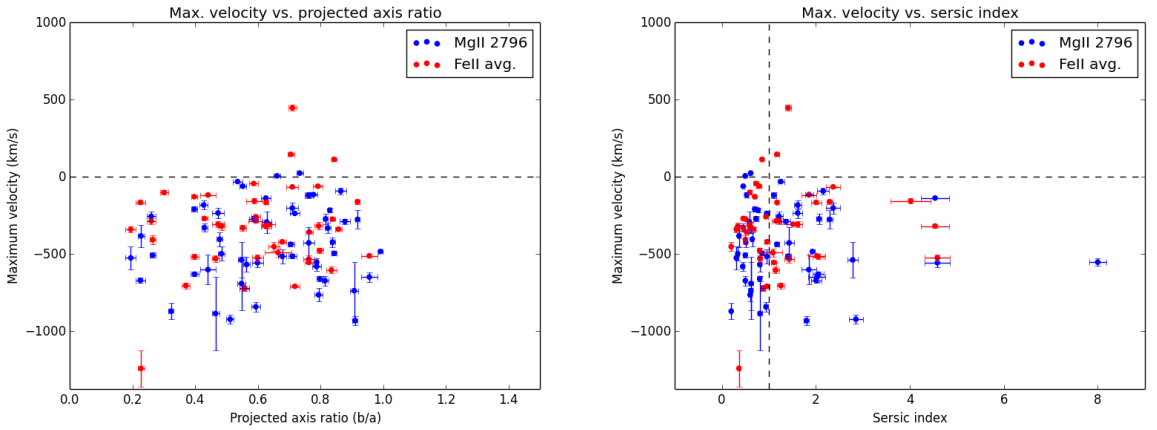

(c) (d)

Figure 3.6: Plots of maximum velocity against the van der Wel data.

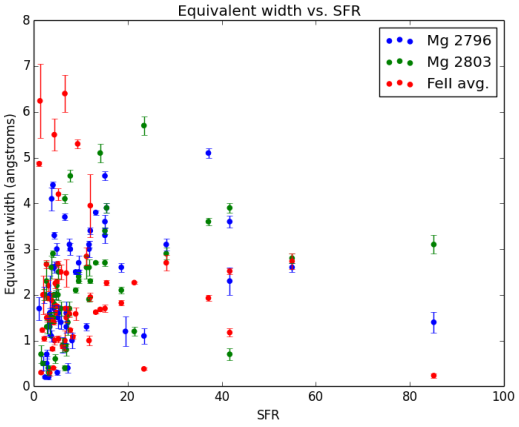

(a)

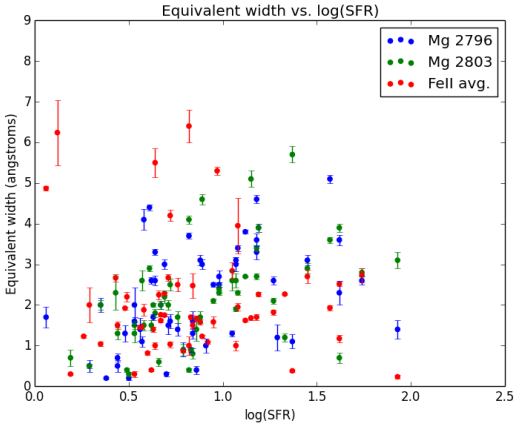

(b)

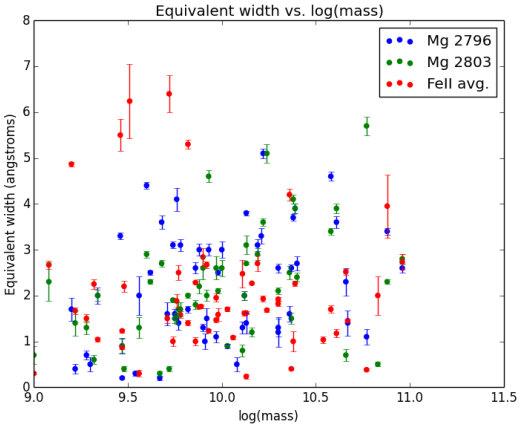

(c)

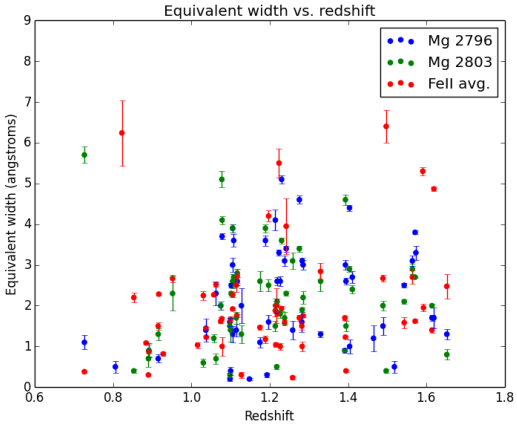

(d)

Figure 3.7: Plots of equivalent width.

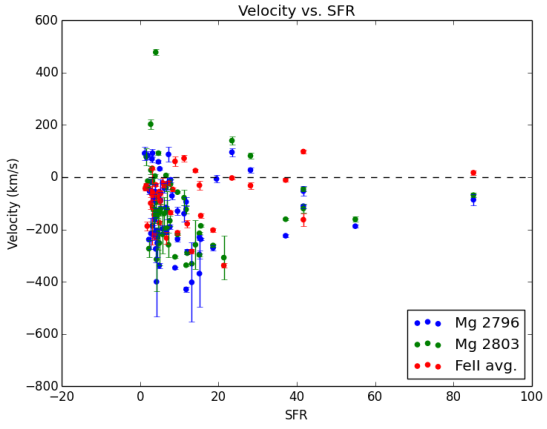

(a)

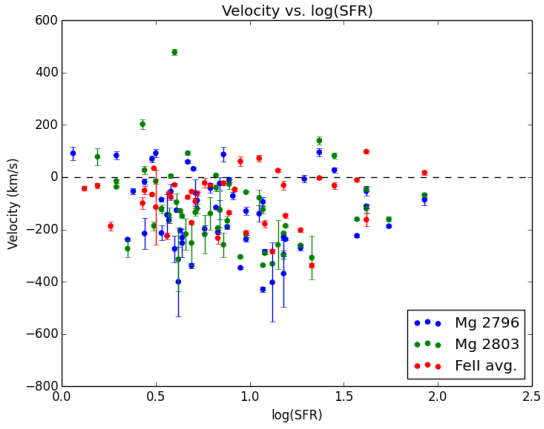

(b)

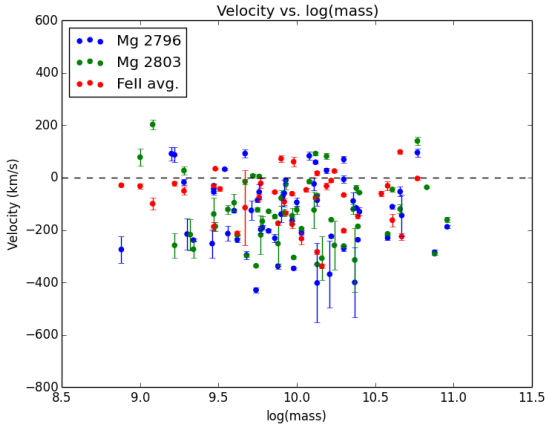

(c)

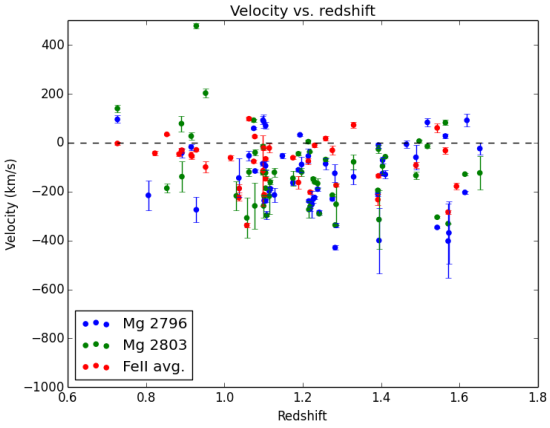

(d)

Figure 3.8: Plots of velocity.

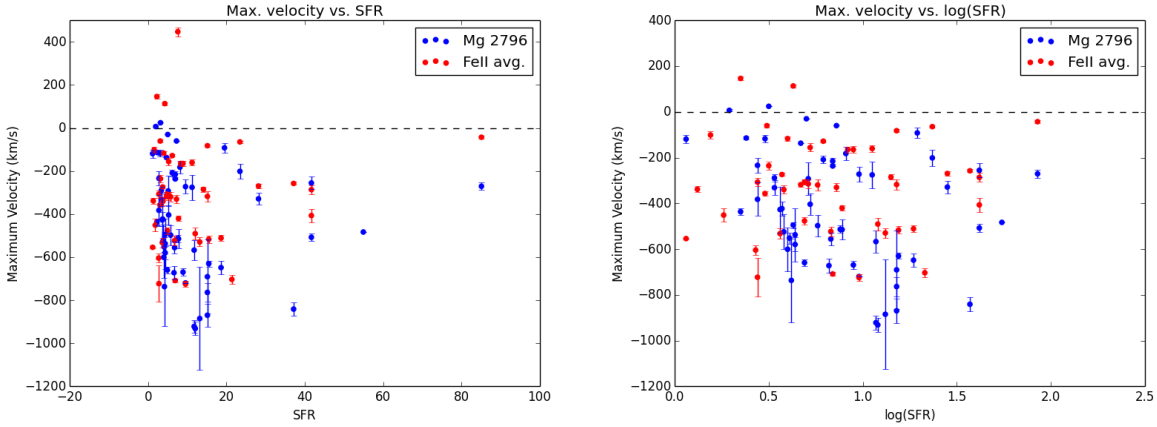

(a)

(b)

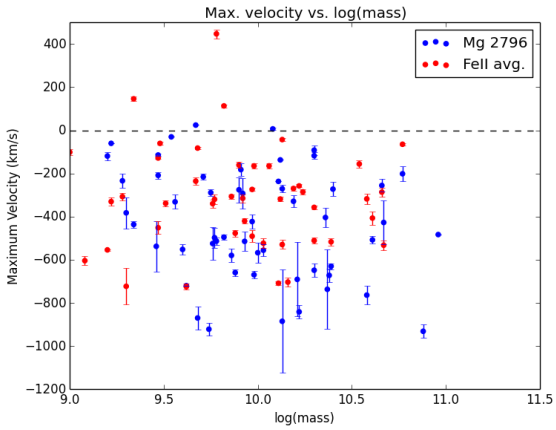

(c)

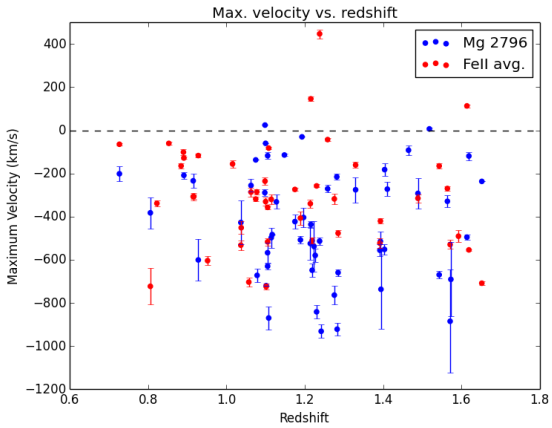

(d)

Figure 3.9: Plots of maximum velocity.

Object	FeII 2249.88	FeII 2260.78	FeII 2344.21	FeII 2374.46	FeII 2382.76	FeII 2586.65	FeII 2600.17	MgII 2796.35	MgII 2803.53
001.COS9419	<0.3	1.8 ±0.5	1.5 ±0.3	0.7 ±0.2	<1.5	<1.2	1.2 ±0.2	1.3 ±0.3	<3.0
002.COS11696	<0.3	<0.3	<0.9	<0.3	<0.3	<1.2	<4.5	<1.8	...
004.COS11968	<0.9	<18.9	1.4 ±0.4	<0.9	<0.6	<0.6	<0.9	<3.9	<0.6
005.COS14214	<0.3	<0.6	2.2 ±0.4	3.1 ±0.2	3.8 ±0.2	2.1 ±0.4	2.3 ±0.3	4.4 ±0.3	2.9 ±0.3
007.COS23287	<0.6	<0.3	0.7 ±0.2	<0.9	<0.9	<0.3	<0.3	<4.2	<0.6
009.COS25927	<0.3	<1.2	<4.2	<1.5	1.7 ±0.4	<1.8	2.0 ±0.4	<2.1	<2.1
010.COS26382	<0.9	<4.8	1.7 ±0.5	<0.6	<0.9	<1.2	<0.6	2.7 ±0.6	2.4 ±0.4
024.COS4275	...	...	...	...	...	<1.2	<2.4	<5.1	<0.6
025.COS5191	...	...	...	<0.3	1.1 ±0.1	<1.5	<2.1	3.3 ±0.3	<5.7
026.COS7167	<4.2	<0.6	<0.6	<0.6	0.9 ±0.3	<2.4	<3.9	<0.6	<6.6
028.COS9352	...	...	...	...	...	<0.3	<0.9	<0.6	<0.6
029.COS10153	<0.3	...	<0.6	<1.5	<0.3	<0.6	<0.9	<0.3	<0.3
033.COS13739	...	...	<1.8	<2.7	1.5 ±0.4	1.9 ±0.6	1.2 ±0.4	<1.8	<1.8
034.COS15852	<0.6	<1.8	<6.6	<2.7	<2.4	<3.3	2.4 ±0.7	<2.1	2.0 ±0.5
035.COS16172	...	...	...	...	...	1.9 ±0.6	2.6 ±0.6	3.6 ±0.5	3.9 ±0.4
038.COS22785	<3.3	<2.7	<0.9	<0.9	<0.9	<1.5	<2.1	<2.7	<1.2
039.COS22854	...	...	<0.9	<1.2	<1.8	<1.5	<1.5	4.1 ±1.0	1.5 ±0.5
040.COS25161	<0.9	<4.2	<2.1	<6.6	<5.1	2.9 ±0.8	3.2 ±0.8	3.1 ±0.5	<1.6
041.COS27996	...	...	...	...	...	...	...	<2.7	3.1 ±0.8
042.COS29589	...	...	...	<1.5	<1.2	<3.9	<3.9	<5.1	<2.7
044.COS6327	...	...	...	...	...	...	...	...	<2.1
045.COS10318	...	...	...	...	...	<13.8	5.5 ±1.4	3.6 ±0.6	2.7 ±0.3
046.COS13403	...	...	...	...	...	<5.1	<15.0	<1.8	<1.2
047.COS18951	...	...	...	...	...	...	...	<19.8	...
048.COS21048	...	...	...	...	...	...	...	<1.2	<1.2
050.COS23890	...	...	...	...	...	12.2 ±3.2	0.6 ±0.2	<2.1	5.7 ±0.8
051.COS25407	...	...	...	...	<21.6	<3.0	2.0 ±0.5	<1.5	<5.7
052.COS27873	...	...	...	...	...	...	...	<1.8	<0.6
054.COS17114	...	...	...	...	...	<1.5	...	<2.1	<2.4
056.COS20100	<0.9	<2.7	<6.9	<2.7	<6.0	<4.5	<5.7	<2.1	<1.8

Table 3.2: Equivalent width measurements (in angstroms) for the COS data.

Object	FeII 2249.88	FeII 2260.78	FeII 2344.21	FeII 2374.46	FeII 2382.76	FeII 2586.65	FeII 2600.17	MgII 2796.35	MgII 2803.53
000.EGS613	<0.6	...	2.2 ±0.5	1.5 ±0.4	3.8 ±0.7	1.8 ±0.3	2.0 ±0.5	5.1 ±0.4	3.6 ±0.3
002.EGS1684	<0.6	<0.3	2.0 ±0.4	1.8 ±0.5	1.3 ±0.4	1.6 ±0.3	1.7 ±0.4	<2.7	2.0 ±0.5
003.EGS2838	<3.3	<0.6	<2.7	2.4 ±0.5	<2.4	<1.8	1.6 ±0.4	2.6 ±0.5	1.8 ±0.4
004.EGS2986	<2.1	<3.0	2.9 ±0.4	<3.3	<4.8	<1.5	<1.8	1.6 ±0.4	1.5 ±0.4
006.EGS6860	<2.4	<0.6	<5.1	<0.6	<0.3	2.8 ±0.5	4.2 ±0.4	2.5 ±0.2	2.3 ±0.2
007.EGS7604	3.4 ±0.3	<0.3	...	<4.8	<1.5	1.5 ±0.3	2.2 ±0.4	3.0 ±0.7	2.6 ±0.7
008.EGS7624	<2.8	<4.8	<4.2	<1.5	<1.8	<2.4	<1.5	<2.1	2.5 ±0.6
009.EGS11029	...	..	4.7 ±0.3	<0.3	6.1 ±0.2	<4.5	3.8 ±0.5	3.7 ±0.3	4.1 ±0.4
011.EGS12858	...	...	<2.1	<1.2	<1.5	2.2 ±0.5	2.2 ±0.5	<2.4	<4.2
013.EGS13376	...	...	<13.8	<10.2	<3.9	<1.8	<2.1	<1.5	<3.0
014.EGS13466	...	...	<0.9	...	...	<2.1	<1.8	<3.3	<3.6
015.EGS14096	<3.3	<1.5	2.4 ±0.8	<2.1	<2.1	1.8 ±0.5	<4.5	3.0 ±0.5	2.2 ±0.6
016.EGS14380	...	...	...	...	...	1.5 ±0.5	<1.8	2.0 ±0.4	2.0 ±0.4
017.EGS14536	<0.3	<0.9	2.7 ±0.3	2.2 ±0.2	2.5 ±0.2	2.5 ±0.2	3.4 ±0.2	3.8 ±0.2	2.7 ±0.1
020.EGS16165	<1.5	<3.9	<1.2	<1.2	<1.5	1.7 ±0.3	1.6 ±0.3	3.4 ±0.3	2.3 ±0.2
022.EGS17348	<8.7	<3.0	4.2 ±0.9	<0.9	<1.8	1.7 ±0.4	<0.9	2.6 ±0.4	2.1 ±0.3
024.EGS18728	<0.9	<0.9	3.8 ±0.7	<1.5	1.7 ±0.4	3.5 ±0.7	4.4 ±0.8	3.1 ±0.5	2.9 ±0.5
025.EGS18959	...	...	...	<0.3	<0.3	...	0.4 ±0.1	0.9 ±0.2	0.9 ±0.1
026.EGS19027	...	...	<3.6	<1.5	<1.8	<1.2	<3.6	<0.3	<0.9
027.EGS19878	<0.9	<0.9	1.9 ±0.4	<1.2	<1.8	1.6 ±0.4	1.9 ±0.5	3.3 ±0.7	<0.6
028.EGS20371	...	...	<0.6	<4.8	<2.4	2.2 ±0.5	<2.1	2.6 ±0.4	2.8 ±0.4
030.EGS24018	...	...	...	...	...	<1.2	<1.8	<0.9	<0.6
031.EGS24533	...	...	1.5 ±0.3	1.3 ±0.3	1.6 ±0.3	2.0 ±0.5	2.4 ±0.3	3.1 ±0.3	1.9 ±0.2
032.EGS25075	<1.5	<0.9	1.5 ±0.4	<0.9	<1.8	3.4 ±0.5	3.2 ±0.4	2.6 ±0.3	1.5 ±0.5
034.EGS26698	<8.4	<10.8	<7.2	<3.3	<3.0	<3.3	<3.3	<3.6	<1.5
035.EGS27622	<4.5	<0.6	<1.2	<1.5	<1.8	2.1 ±0.6	4.1 ±0.5	4.6 ±0.4	3.4 ±0.3
037.EGS29026	...	...	...	...	...	<16.5	3.1 ±0.5	3.0 ±0.5	4.6 ±0.5
043.EGS13891	<0.9	<0.6	2.0 ±0.3	1.2 ±0.3	<1.2	1.8 ±0.3	2.1 ±0.3	<6.9	1.2 ±0.4
045.EGS16966	<1.2	<3.3	<2.4	1.2 ±0.4	1.6 ±0.5	2.1 ±0.5	2.2 ±0.5	<3.0	<1.2
046.EGS17596	<0.6	<0.9	2.7 ±0.3	2.0 ±0.4	2.0 ±0.4	1.7 ±0.3	1.6 ±0.4	...	...
048.EGS19286	<0.3	<1.5	2.0 ±0.3	1.4 ±0.3	1.3 ±0.3	1.5 ±0.3	2.0 ±0.3	<0.3	<0.6
049.EGS20805	<2.1	<3.6	1.7 ±0.4	<1.5	<1.8	2.1 ±0.5	1.7 ±0.5	<1.5	<1.5
050.EGS24454	<0.9	<0.3	2.8 ±0.5	1.7 ±0.4	1.5 ±0.3	1.6 ±0.3	2.0 ±0.3	1.7 ±0.3	2.0 ±0.2
053.EGS7213	...	...	...	...	...	<2.7	<1.8	<3.0	<3.0
054.EGS19178	...	...	...	...	...	3.7 ±0.7	4.7 ±0.8	2.5 ±0.2	2.1 ±0.2
056.EGS9413	...	...	...	...	...	3.8 ±0.7	9.5 ±0.8	<1.2	<3.0
057.EGS9704	...	<6.3	<4.2	<9.9	<12.6	<5.4	<5.4	<2.1	<5.1
058.EGS14844	...	...	2.7 ±0.6	4.4 ±0.5	...	<1.8	3.1 ±0.9	<1.2	<1.8
060.EGS20005	...	...	...	...	...	<1.5	1.6 ±0.5	<1.2	<3.3
061.EGS25861	<1.5	<3.9	3.5 ±0.5	<1.5	4.1 ±1.0	4.3 ±0.9	3.8 ±1.2	<2.1	5.1 ±0.8
062.EGS27539	<2.1	<1.5	2.9 ±0.6	3.3 ±0.6	<2.4	<2.4	2.4 ±0.6	3.9 ±0.4	3.9 ±0.4

Table 3.3: Equivalent width measurements (in angstroms) for the EGS data.

Object	SFR ($M_{\odot}yr^{-1}$)	log(mass) ($M/M_{\odot}$)	R magnitude	Redshift
001.COS9419	11.22	9.90	23.66	1.3298
002.COS11696	1.95	10.08	23.77	1.5182
004.COS11968	19.50	10.30	23.94	1.4649
005.COS14214	4.07	9.60	23.56	1.4036
007.COS23287	6.61	9.72	23.95	1.4972
009.COS25927	8.13	9.91	23.55	1.4039
010.COS26382	9.55	10.40	23.79	1.4108
024.COS4275	1.95	10.83	23.99	1.2178
025.COS5191	4.37	9.46	23.81	1.2236
026.COS7167	5.01	9.54	23.91	1.1929
028.COS9352	3.16	9.67	23.84	1.0985
029.COS10153	2.40	9.47	23.98	1.1480
033.COS13739	5.75	9.77	23.33	1.1144
034.COS15852	2.24	9.34	23.92	1.2155
035.COS16172	41.69	10.61	22.47	1.1889
038.COS22785	4.57	9.32	23.64	1.0303
039.COS22854	3.80	9.76	24.00	1.2142
040.COS25161	7.59	9.78	23.67	1.2379
041.COS27996	85.11	10.13	23.92	1.2584
042.COS29589	3.39	9.56	23.83	1.1275
044.COS6327	5.25	10.54	22.93	1.0156
045.COS10318	15.14	9.68	23.16	1.1079
046.COS13403	2.75	9.30	23.63	0.8057
047.COS18951	3.98	8.88	23.39	0.9281
048.COS21048	8.32	10.06	23.26	0.8842
050.COS23890	23.44	10.77	22.09	0.7267
051.COS25407	4.90	9.86	23.84	0.9167
052.COS27873	3.09	9.48	23.36	0.8529
054.COS17114	1.55	9.00	24.28	0.8902
056.COS20100	6.17	9.47	24.38	0.8913

Table 3.4: Table showing SFR, log(mass), R magnitude, and redshift of the COS objects from the 3D-HST catalogue.

Object	SFR ($M_{\odot}yr^{-1}$)	log(mass) ($M/M_{\odot}$)	R magnitude	Redshift
000.EGS613	37.15	10.22	23.43	1.2302
002.EGS1684	5.13	9.92	23.70	1.4890
003.EGS2838	4.37	9.86	23.68	1.2267
004.EGS2986	3.39	9.75	23.97	1.0980
006.EGS6860	9.55	9.62	22.83	1.1015
007.EGS7604	11.75	10.00	23.49	1.1050
008.EGS7624	5.25	10.36	23.46	1.1970
009.EGS11029	6.61	10.38	23.21	1.0783
011.EGS12858	3.02	10.30	23.45	1.1052
013.EGS13376	3.72	9.97	23.89	1.1749
014.EGS13466	3.63	10.67	23.35	1.0368
015.EGS14096	4.90	9.88	23.91	1.2851
016.EGS14380	4.68	10.12	23.92	1.0748
017.EGS14536	13.18	10.13	23.13	1.5712
020.EGS16165	12.02	10.88	23.14	1.2419
022.EGS17348	18.62	10.30	23.34	1.2188
024.EGS18728	28.18	10.19	23.98	1.5642
025.EGS18959	6.76	10.03	23.58	1.3918
026.EGS19027	4.68	9.89	23.27	1.1159
027.EGS19878	15.14	10.21	23.92	1.5731
028.EGS20371	54.95	10.96	23.35	1.1169
030.EGS24018	1.82	9.47	23.87	1.0377
031.EGS24533	11.75	9.74	23.46	1.2827
032.EGS25075	4.17	10.37	23.39	1.3946
034.EGS26698	41.69	10.66	23.93	1.0627
035.EGS27622	15.14	10.58	23.75	1.2755
037.EGS29026	7.76	9.93	23.78	1.3932
043.EGS13891	21.38	10.16	23.91	1.0571
045.EGS16966	6.92	9.71	23.92	1.2818
046.EGS17596	12.02	9.97	23.22	1.5925
048.EGS19286	9.33	9.82	23.70	1.5907
049.EGS20805	6.92	10.11	23.93	1.6521
050.EGS24454	4.27	9.82	23.93	1.6141
053.EGS7213	1.15	9.20	23.96	1.6191
054.EGS19178	8.91	9.98	22.91	1.5432
056.EGS9413	1.32	9.51	24.18	0.8224
057.EGS9704	2.69	9.08	24.32	0.9518
058.EGS14844	2.75	9.28	24.12	0.9151
060.EGS20005	7.24	9.22	24.03	1.1000
061.EGS25861	14.13	10.24	24.06	1.0775
062.EGS27539	15.49	10.39	24.05	1.1051

Table 3.5: Table showing various properties of the EGS objects from the 3D-HST catalogue.

Plot	Spearman coefficient
Fig 3.7(a) ew vs sfr	3.2
Fig 3.7(b) ew vs log(sfr)	3.2
Fig 3.7(c) ew vs log(mass)	1.8
Fig 3.7(d) ew vs redshift	2.4
Fig 3.4(a) ew vs semi-major axis	2.2
Fig 3.4(b) ew vs log(sma)	2.2
Fig 3.4(c) ew vs projected axis ratio	0.2
Fig 3.4(d) ew vs sersic	1.1
Fig 3.8(a) velocity vs sfr	2.6
Fig 3.8(b) velocity vs log(sfr)	2.6
Fig 3.8(c) velocity vs log(mass)	1.3
Fig 3.8(d) velocity vs redshift	0.6
Fig 3.5(a) velocity vs semi-major axis	0.5
Fig 3.5(b) velocity vs log(sma)	0.5
Fig 3.5(c) velocity vs projected axis ratio	0.1
Fig 3.5(d) velocity vs sersic	0.0
Fig 3.9(a) maxv vs sfr	2.7
Fig 3.9(b) maxv vs log(sfr)	2.7
Fig 3.9(c) maxv vs log(mass)	1.9
Fig 3.9(d) maxv vs z	0.4
Fig 3.6(a) maxv vs semi-major axis	0.5
Fig 3.6(b) maxv vs log(sma)	0.5
Fig 3.6(c) maxv vs projected axis ratio	0.1
Fig 3.6(d) maxv vs sersic	0.8

Table 3.6: A table of the Spearman correlation coefficients of each of the plots.

width of MgII absorption was greater in galaxies with higher SFRs.

3.2 Conclusions

As predicted by the models and observations discussed in the introduction, we found that outflows are common in galaxies at $1<z<2$, suggesting that outflows can indeed be used to explain the baryon deficit in these galaxies and the enrichment of the IGM. Our observations show a correlation between the equivalent width of the absorption lines and SFR. Unlike Heckman et al. (2015) and Martin (2005), we found no correlation with outflow velocity and any other property. There also appears to be no

relationship between galactic axis ratio and outflow velocity, suggesting that the lack of correlation between outflow velocity and inclination at $z \sim 2$ found by Law et al. (2012) is also present in our lower redshift galaxy sample.

There are a variety of reasons why trends might not be visible. It's possible that our sample doesn't have enough range in some of the parameters, which Chen et al. (2010) suggest might explain the lack of trends in their observations. Trends might be more obvious if we had more galaxies with a greater range of magnitudes. Also, multi-component modeling with programs like GALFIT might be able to more accurately fit the galaxies, and enable us to better distinguish disks by separating them from other components, like bulges. This would make clear any possible trends in the semi-major axis, projected axis ratio, and Sersic index. Future work will try to take all of this into account to further investigate correlations between outflows and galaxy properties.

Bibliography

Aguirre, A., Hernquist, L., Schaye, J., Weinberg, D. H., Katz, N., & Gardner, J. 2001, ApJ, 560, 599

Chen, Y.-M., Tremonti, C. A., Heckman, T. M., Kauffmann, G., Weiner, B. J., Brinchmann, J., & Wang, J. 2010, AJ, 140, 445

Choi, E., Ostriker, J. P., Naab, T., Somerville, R. S., Hirschmann, M., Núñez, A., Hu, C.-Y., & Oser, L. 2016, ArXiv e-prints

Cooper, M. C., Newman, J. A., Davis, M., Finkbeiner, D. P., & Gerke, B. F. 2012, spec2d: DEEP2 DEIMOS Spectral Pipeline, Astrophysics Source Code Library

Dalcanton, J. J. 2007, ApJ, 658, 941

Erb, D. K., Quider, A. M., Henry, A. L., & Martin, C. L. 2012, ApJ, 759, 26

Faber, S. M., Phillips, A. C., Kibrick, R. I., Alcott, B., Allen, S. L., Burrous, J., Cantrall, T., Clarke, D., Coil, A. L., Cowley, D. J., Davis, M., Deich, W. T. S., Dietsch, K., Gilmore, D. K., Harper, C. A., Hilyard, D. F., Lewis, J. P., McVeigh, M., Newman, J., Osborne, J., Schiavon, R., Stover, R. J., Tucker, D., Wallace, V., Wei, M., Wirth, G., & Wright, C. A. 2003, in Proc. SPIE, Vol. 4841, Instrument Design and Performance for Optical/Infrared Ground-based Telescopes, ed. M. Iye & A. F. M. Moorwood, 1657–1669

Grogin, N. A., Kocevski, D. D., Faber, S. M., Ferguson, H. C., Koekemoer, A. M., Riess, A. G., Acquaviva, V., Alexander, D. M., Almaini, O., Ashby, M. L. N., Barden, M., Bell, E. F., Bournaud, F., Brown, T. M., Caputi, K. I., Casertano, S., Cassata, P., Castellano, M., Challis, P., Chary, R.-R., Cheung, E., Cirasuolo, M., Conselice, C. J., Roshan Cooray, A., Croton, D. J., Daddi, E., Dahlen, T., Davé, R., de Mello, D. F., Dekel, A., Dickinson, M., Dolch, T., Donley, J. L., Dunlop, J. S., Dutton, A. A., Elbaz, D., Fazio, G. G., Filippenko, A. V., Finkelstein, S. L., Fontana, A., Gardner, J. P., Garnavich, P. M., Gawiser, E., Giavalisco, M., Grazian, A., Guo, Y., Hathi, N. P., Häussler, B., Hopkins, P. F., Huang, J.-S., Huang, K.-H., Jha, S. W., Kartaltepe, J. S., Kirshner, R. P., Koo, D. C., Lai, K., Lee, K.-S., Li, W., Lotz, J. M., Lucas, R. A., Madau, P., McCarthy, P. J., McGrath, E. J., McIntosh, D. H., McLure, R. J., Mobasher, B., Moustakas, L. A., Mozena, M., Nandra, K., Newman, J. A., Niemi, S.-M., Noeske, K. G., Papovich, C. J., Pentericci, L., Pope, A., Primack, J. R., Rajan, A., Ravindranath, S., Reddy, N. A., Renzini, A., Rix, H.-W., Robaina, A. R., Rodney, S. A., Rosario, D. J., Rosati, P., Salimbeni, S., Scarlata, C., Siana, B., Simard, L., Smidt, J., Somerville, R. S., Spinrad, H., Straughn, A. N., Strolger, L.-G., Telford, O., Teplitz, H. I., Trump, J. R., van der Wel, A., Villforth, C., Wechsler, R. H., Weiner, B. J., Wiklind, T., Wild, V., Wilson, G., Wuyts, S., Yan, H.-J., & Yun, M. S. 2011, ApJS, 197, 35

Heckman, T. M. 2002, in Astronomical Society of the Pacific Conference Series, Vol. 254, Extragalactic Gas at Low Redshift, ed. J. S. Mulchaey & J. T. Stocke, 292

Heckman, T. M., Alexandroff, R. M., Borthakur, S., Overzier, R., & Leitherer, C. 2015, ApJ, 809, 147

Hopkins, P. F., Quataert, E., & Murray, N. 2012, MNRAS, 421, 3522

Kennicutt, Jr., R. C. 1998, ApJ, 498, 541

Kereš, D., Katz, N., Davé, R., Fardal, M., & Weinberg, D. H. 2009a, MNRAS, 396, 2332

Kereš, D., Katz, N., Fardal, M., Davé, R., & Weinberg, D. H. 2009b, MNRAS, 395, 160

Koekemoer, A. M., Faber, S. M., Ferguson, H. C., Grogin, N. A., Kocevski, D. D., Koo, D. C., Lai, K., Lotz, J. M., Lucas, R. A., McGrath, E. J., Ogaz, S., Rajan, A., Riess, A. G., Rodney, S. A., Strolger, L., Casertano, S., Castellano, M., Dahlen, T., Dickinson, M., Dolch, T., Fontana, A., Giavalisco, M., Grazian, A., Guo, Y., Hathi, N. P., Huang, K.-H., van der Wel, A., Yan, H.-J., Acquaviva, V., Alexander, D. M., Almaini, O., Ashby, M. L. N., Barden, M., Bell, E. F., Bournaud, F., Brown, T. M., Caputi, K. I., Cassata, P., Challis, P. J., Chary, R.-R., Cheung, E., Cirasuolo, M., Conselice, C. J., Roshan Cooray, A., Croton, D. J., Daddi, E., Davé, R., de Mello, D. F., de Ravel, L., Dekel, A., Donley, J. L., Dunlop, J. S., Dutton, A. A., Elbaz, D., Fazio, G. G., Filippenko, A. V., Finkelstein, S. L., Frazer, C., Gardner, J. P., Garnavich, P. M., Gawiser, E., Gruetzbauch, R., Hartley, W. G., Häussler, B., Herrington, J., Hopkins, P. F., Huang, J.-S., Jha, S. W., Johnson, A., Kartaltepe, J. S., Khostovan, A. A., Kirshner, R. P., Lani, C., Lee, K.-S., Li, W., Madau, P., McCarthy, P. J., McIntosh, D. H., McLure, R. J., McPartland, C., Mobasher, B., Moreira, H., Mortlock, A., Moustakas, L. A., Mozena, M., Nandra, K., Newman, J. A., Nielsen, J. L., Niemi, S., Noeske, K. G., Papovich, C. J., Pentericci, L., Pope, A., Primack, J. R., Ravindranath, S., Reddy, N. A., Renzini, A., Rix, H.-W., Robaina, A. R., Rosario, D. J., Rosati, P., Salimbeni, S., Scarlata, C., Siana, B., Simard, L., Smidt, J., Snyder, D., Somerville, R. S., Spinrad, H., Straughn, A. N., Telford, O., Teplitz, H. I., Trump, J. R., Vargas, C., Villforth, C., Wagner, C. R., Wandro, P., Wechsler, R. H., Weiner, B. J., Wiklind, T., Wild, V., Wilson, G., Wuyts, S., & Yun, M. S. 2011, ApJS, 197, 36

Kornei, K. A., Shapley, A. E., Martin, C. L., Coil, A. L., Lotz, J. M., Schiminovich, D., Bundy, K., & Noeske, K. G. 2012, ApJ, 758, 135

Kornei, K. A., Shapley, A. E., Martin, C. L., Coil, A. L., Lotz, J. M., & Weiner, B. J. 2013, ApJ, 774, 50

Law, D. R., Steidel, C. C., Shapley, A. E., Nagy, S. R., Reddy, N. A., & Erb, D. K. 2012, ApJ, 759, 29

Martin, C. L. 2005, ApJ, 621, 227

Martin, C. L., Shapley, A. E., Coil, A. L., Kornei, K. A., Bundy, K., Weiner, B. J., Noeske, K. G., & Schiminovich, D. 2012, ApJ, 760, 127

Muratov, A. L., Kereš, D., Faucher-Giguère, C.-A., Hopkins, P. F., Quataert, E., & Murray, N. 2015, MNRAS, 454, 2691

Murray, N., Ménard, B., & Thompson, T. A. 2011, ApJ, 735, 66

Murray, N., Quataert, E., & Thompson, T. A. 2005, ApJ, 618, 569

Newman, J. A., Cooper, M. C., Davis, M., Faber, S. M., Coil, A. L., Guhathakurta, P., Koo, D. C., Phillips, A. C., Conroy, C., Dutton, A. A., Finkbeiner, D. P., Gerke, B. F., Rosario, D. J., Weiner, B. J., Willmer, C. N. A., Yan, R., Harker, J. J., Kassin, S. A., Konidaris, N. P., Lai, K., Madgwick, D. S., Noeske, K. G., Wirth, G. D., Connolly, A. J., Kaiser, N., Kirby, E. N., Lemaux, B. C., Lin, L., Lotz, J. M., Luppino, G. A., Marinoni, C., Matthews, D. J., Metevier, A., & Schiavon, R. P. 2013, ApJS, 208, 5

Oesch, P. A., Carollo, C. M., Feldmann, R., Hahn, O., Lilly, S. J., Sargent, M. T., Scarlata, C., Aller, M. C., Aussel, H., Bolzonella, M., Bschorr, T., Bundy, K., Capak, P., Ilbert, O., Kneib, J.-P., Koekemoer, A. M., Kovač, K., Leauthaud, A., Le Floc'h, E., Massey, R., McCracken, H. J., Pozzetti, L., Renzini, A., Rhodes, J.,

Salvato, M., Sanders, D. B., Scoville, N., Sheth, K., Taniguchi, Y., & Thompson, D. 2010, ApJ, 714, L47

Prochaska, J. X., Kasen, D., & Rubin, K. 2011, ApJ, 734, 24

Shapley, A. E. 2011, ARAA, 49, 525

Silk, J. 2003, MNRAS, 343, 249

Skelton, R. E., Whitaker, K. E., Momcheva, I. G., Brammer, G. B., van Dokkum, P. G., Labbé, I., Franx, M., van der Wel, A., Bezanson, R., Da Cunha, E., Fumagalli, M., Förster Schreiber, N., Kriek, M., Leja, J., Lundgren, B. F., Magee, D., Marchesini, D., Maseda, M. V., Nelson, E. J., Oesch, P., Pacifici, C., Patel, S. G., Price, S., Rix, H.-W., Tal, T., Wake, D. A., & Wuyts, S. 2014, ApJS, 214, 24

Steidel, C. C., Erb, D. K., Shapley, A. E., Pettini, M., Reddy, N., Bogosavljević, M., Rudie, G. C., & Rakic, O. 2010, ApJ, 717, 289

Tremonti, C. A., Heckman, T. M., Kauffmann, G., Brinchmann, J., Charlot, S., White, S. D. M., Seibert, M., Peng, E. W., Schlegel, D. J., Uomoto, A., Fukugita, M., & Brinkmann, J. 2004, ApJ, 613, 898

Weiner, B. J., Coil, A. L., Prochaska, J. X., Newman, J. A., Cooper, M. C., Bundy, K., Conselice, C. J., Dutton, A. A., Faber, S. M., Koo, D. C., Lotz, J. M., Rieke, G. H., & Rubin, K. H. R. 2009, ApJ, 692, 187